Enhancing oxygen permeation of solid-state reactive sintered $Ce_{0.8}Gd_{0.2}O_{2-\delta}$-$FeCo_2O_4$ composite by optimizing the powder preparation method

Fanlin Zeng[1,2,*], Stefan Baumann[1], Jürgen Malzbender[1], Arian Nijmeijer[2], Louis Winnubst[2], Olivier Guillon[1], Ruth Schwaiger[1,3], Wilhelm A. Meulenberg[1,2]

[1]Forschungszentrum Jülich GmbH, Institute of Energy and Climate Research (IEK), 52425 Jülich, Germany
[2]University of Twente, Faculty of Science and Technology, Inorganic Membranes, P.O. Box 217, 7500 AE Enschede, The Netherlands
[3]RWTH Aachen University, Chair of Energy Engineering Materials, 52056 Aachen, Germany

Abstract

Dual phase membranes with mixed ionic-electronic conductivity exhibit promising properties for applications in pure oxygen separation under harsh atmospheres. The conductivity of an individual phase within dual phase membranes is often attenuated by the blocking effects from the other phase(s). Here, facile but effective ways are reported to alleviate such effects by optimizing the powder preparation method for a solid-state reactive sintering process. Powder mixtures with a nominal composition 85 wt% $Ce_{0.8}Gd_{0.2}O_{2-\delta}$:15 wt% $FeCo_2O_4$ were prepared by traditional wet ball milling method, as well as a moderate dry mixing approach. Using a modified wet ball milling procedure, homogenous powder mixtures with fine particle size are obtained and the synthesized membrane shows a fine and homogenous microstructure that realizes high oxygen permeance. Besides, a novel "dual phase" membrane having one ionic conductive monophase zone and one mixed ionic-electronic multiphase zone was sintered using dry-mixed powder mixtures. With individual mesoscale percolations, two phase zones provide relatively straight paths for ionic conduction and electronic conduction, respectively, which contributes to achieving the highest oxygen permeance among all the sintered membranes.

Keywords: dual phase oxygen transport membrane; powder preparation; grain size; homogeneity; oxygen permeation

1. Introduction

Ceramic oxygen permeation membranes, which are composed of mixed ionic-electronic conducting ceramic oxides, have been developed for in situ separation of oxygen for use in clean energy schemes such as pre-combustion carbon capture, and oxyfuel technology for power plants [1-5]; these applications entail a harsh atmosphere containing CO_2, H_2O and traces of SO_2 [6], which challenges the stability of the membrane materials. The typical high permeable perovskite-type membrane materials, e.g., $Ba_{0.5}Sr_{0.5}Co_{0.8}Fe_{0.2}O_{3-\delta}$ and $La_{0.6}Sr_{0.4}Co_{0.2}Fe_{0.8}O_{3-\delta}$ [7, 8], suffer from irreversible material deteriorations due to carbonating and sulfating reactions. Furthermore, these perovskite oxides also suffer from mechanical instability, e.g., cracking and delamination, caused by their high thermal and chemical expansion [9, 10].

*Corresponding author
Email: f.zeng@fz-juelich.de
Tel.: ++49-2461-619399
Fax: ++49-2461-612455

By contrast, some dual phase membranes exhibit high stability under the CO_2- and SO_2-containing environments at high temperatures [11], and hence, they appear to be more attractive candidates than single phase perovskite-type oxides. Dual phase membranes comprise of two different kinds of phases providing ionic conductivity and electronic conductivity, respectively. Fluorite oxides, e.g., gadolinium- or samarium-doped ceria, and yttria-stabilized zirconia, are often chosen as the ionic conducting phase for dual phase membranes because of their high ionic conductivity as well as high chemical stability in an acidic atmosphere [12-14]; spinel oxides, e.g., $Fe_xCo_{3-x}O_4$ (x = 1 or 2), $NiFe_2O_4$, and $Mn_{1.5}Co_{1.5}O_4$, have attracted considerable attention as suitable electronic conducting phases combined with fluorite oxides to form robust high-performance dual phase membranes [6, 11, 15-17]. As an example, 85 wt% $Ce_{0.8}Gd_{0.2}O_{2-\delta}$-15 wt% $FeCo_2O_4$ composite, which consists of a $Ce_{1-x}Gd_xO_{2-\delta}$ ($0 < x < 0.2$) (CGO) fluorite phase, a $Fe_yCo_{3-y}O_4$ ($0 < y < 2$) (FCO) spinel phase and a $Gd_{0.85}Ce_{0.15}Fe_{0.75}Co_{0.25}O_3$ (GCFCO) perovskite phase [15, 18-20], was verified to possess high tolerance over 200 h in CO_2- and SO_2-containing gas mixtures at 850 °C under an oxygen partial pressure gradient [15].

Oxygen permeation through ceramic oxygen permeation membranes can be classified into two kinds of processes [21]: gas-solid interfacial exchange at the surface (surface exchange) and ion/electron diffusion in the bulk. For a dual phase membranes comprising two kinds of phases possessing pure ionic conductivity and pure electronic conductivity, respectively, the surface exchange only takes place at triple phase boundaries (TPBs) [22], which are the connection lines of ionic conducting grains, electronic conducting grains and the gas phase. Thus, to improve the surface exchange, an effective way is to extend the available length of the TPBs by microstructural optimizations, e.g., increasing the homogeneity of the two kinds of phases [23], and reducing the grain size [24], as well as coating a porous activation layer with mixed ionic-electronic conductivity on the surfaces [22].

The bulk diffusion within a dual phase membrane is realized by the ambipolar conductivity, i.e. the ambipolar conduction of ions and electrons through continuous paths formed by the two kinds of phases, respectively [21]. The ambipolar conductivity (σ_{amb}) can be expressed as [18]:

$$\sigma_{amb} = \frac{\sigma_{p,i} \cdot \sigma_{p,e}}{\sigma_{p,i} + \sigma_{p,e}} \tag{1}$$

where $\sigma_{p,i}$ and $\sigma_{p,e}$ represent the partial ionic conductivity and the partial electronic conductivity, respectively. The partial ionic/electronic conductivity is proportional to the intrinsic ionic/electronic conductivity, as well as the contiguous phase volume transporting ions/electrons through the membrane according to [18].

$$\sigma_{p,i} = \sigma_i \cdot V_{eff,i} \tag{2}$$

$$\sigma_{p,e} = \sigma_e \cdot V_{eff,e} \tag{3}$$

where σ_i and σ_e are the intrinsic ionic and electronic conductivity, respectively. And $V_{eff,i}$ and $V_{eff,e}$ are the continuous volumes providing, respectively, the effective paths for ionic and electronic transport through the membrane. The continuous volume is increasing as a function of the total volume for a randomly distributed phase constituent within a composite [18, 25].

The amount of ionic and electronic conductive phases often needs to be varied to realize a high ambipolar conductivity when intrinsic conductivities of the two kinds of phases do not match. It is essential to increase the volume fraction of the phase with the lowest conductivity but maintain the percolation of the phase with the highest conductivity. In the case that the intrinsic conductivities of two kinds of phases are not of the same order of magnitude, e.g., the ionic conductivity of gadolinium-doped ceria is two orders of magnitude lower than the electronic conductivity of $Fe_xCo_{3-x}O_4$ (x = 1 or 2) [16, 22], the volume fraction of the phase with the highest conductivity should theoretically be lower than 30 vol% to obtain a high ambipolar conductivity and high oxygen permeation flux [18]. For instance, the oxygen permeation fluxes of (1-x) $Ce_{0.8}Gd_{0.2}O_{2-\delta}$-$x$ $FeCo_2O_4$ (10 wt% ≤ x ≤ 40 wt%) composites approach the maximum value when x reaches 15 wt% [15]. Such a small volume, however, is in practice a challenge for the formation of sufficiently continuous networks for electronic conduction. The total conductivity of 85 wt% $Ce_{0.8}Gd_{0.2}O_{2-\delta}$-15 wt% $FeCo_2O_4$ composite is around one order of magnitude lower than that of 70 wt% $Ce_{0.8}Gd_{0.2}O_{2-\delta}$-30 wt% $FeCo_2O_4$ composite [26]. Hence, for composites such as 80 vol% $Ce_{0.8}Gd_{0.2}O_{2-\delta}$-20 vol% $MnCo_{1.9}Fe_{0.1}O_4$ [27], 85 wt% $Ce_{0.8}Gd_{0.2}O_{2-\delta}$-15 wt% $FeCo_2O_4$ [15], and 85 vol% $Ce_{0.8}Gd_{0.2}O_{2-\delta}$-15 vol% $MnCo_2O_4$ [28], electronic conduction, which is realized by a comparably small volume of electronic conducting phases, is believed to be the bottleneck for bulk diffusion during oxygen permeation [26].

The existence of a nano-sized grain boundary phase was reported to contribute to the formation of electronic conductive networks in $Ce_{0.8}Gd_{0.2}O_{2-\delta}$-$MnCo_2O_4$ composite at a low volume of $MnCo_2O_4$ [28]. Besides, it was proven to be effective for a minor phase to form percolations through a dual phase membrane by reducing the grain size and increasing the inhomogeneity. Li et al. [29] investigated the electronic conductivity of 75 wt% $Ce_{0.8}Sm_{0.2}O_{1.9}$-25 wt% $Sm_{0.6}Ca_{0.4}CoO_{3-\delta}$ and 75 wt% $Ce_{0.8}Sm_{0.2}O_{1.9}$-25 wt% $Sm_{0.6}Ca_{0.4}FeO_{3-\delta}$ composites and found that only the latter possessed electronic conductivity that was sufficient for oxygen permeation due to the continuous electronic conducting networks formed by the $Sm_{0.6}Ca_{0.4}FeO_{3-\delta}$ grains that are one order of magnitude smaller than the $Ce_{0.8}Sm_{0.2}O_{1.9}$ grains. A study on 75 wt% $Ce_{0.85}Sm_{0.15}O_{3-\delta}$-25 wt% $Sm_{0.6}Sr_{0.4}FeO_{3-\delta}$ revealed that the grain growth of the major phase, i.e., $Ce_{0.85}Sm_{0.15}O_{3-\delta}$, blocked the connectivity of the minor phase, i.e., $Sm_{0.6}Sr_{0.4}FeO_{3-\delta}$, and yielded a lower oxygen permeation flux [24]. In addition, Zhu et al. [30] used different methods to prepare 75 wt% $Ce_{0.85}Sm_{0.15}O_{1.925}$-25 wt% $Sm_{0.6}Sr_{0.4}Al_{0.3}Fe_{0.7}O_3$ composite and concluded the membrane prepared by solid-state reaction shows the highest oxygen permeation flux and total conductivity due to the inhomogeneous distribution of small $Sm_{0.6}Sr_{0.4}Al_{0.3}Fe_{0.7}O_3$ grains.

Based on the realization of the importance of microstructural aspects regarding grain size and spatial distribution of each phase on the performance of the dual phase membranes, we are motivated to explore facile but effective ways to tailor the microstructural characteristics of dual phase membranes. In this work, the solid-state reactive sintering process was optimized to synthesize composites with a nominal composition 85 wt% $Ce_{0.8}Gd_{0.2}O_{2-\delta}$:15 wt% $FeCo_2O_4$ showing enhanced oxygen permeation. The powder mixtures used for solid-state reactive sintering were prepared by applying different wet ball milling processes on powder mixtures of $Ce_{0.8}Gd_{0.2}O_{2-\delta}$, Co_3O_4 and Fe_2O_3 powders to homogenize the distribution of each compound as well as modify the particle size, which results in homogenous microstructures with different grain sizes for the sintered membranes. Besides, to synthesize a

membrane having the minor conducting phases well connected through the membrane, inhomogeneous powder mixtures were prepared by dry mixing of 50 wt% monophase powders ($Ce_{0.8}Gd_{0.2}O_{2-\delta}$) with fine and homogeneous composite powders having a nominal composition 70 wt% $Ce_{0.8}Gd_{0.2}O_{2-\delta}$:30 wt% $FeCo_2O_4$ in a moderate way. This results in a novel type of composites comprised of a pure ionic conductor ($Ce_{0.8}Gd_{0.2}O_{2-\delta}$) with a mixed ionic-electronic conductor, which is a composite itself (70 wt% $Ce_{0.8}Gd_{0.2}O_{2-\delta}$:30 wt% $FeCo_2O_4$). The nominal overall weight ratio $Ce_{0.8}Gd_{0.2}O_{2-\delta}$:$FeCo_2O_4$ in this composite is again 85:15, so that the properties can directly be compared to the classical composites. The microstructural characteristics and phase constituents of both the classical and the novel composite membranes were analyzed in detail, and their influence on oxygen permeation performance is discussed.

2. Experimental

Dual phase membranes were synthesized by a solid-state reactive sintering process using $Ce_{0.8}Gd_{0.2}O_{2-\delta}$ (Treibacher Industrie AG, 99 %), Co_3O_4 (Alfa Aesar, 99.7 %) and Fe_2O_3 (Sigma-Aldrich, 99 %) as precursor powders; the mole ratio of Co_3O_4 to Fe_2O_3 was fixed at 4:3 to form a nominal compound of $FeCo_2O_4$ during sintering; the weight ratio of ionic conductor ($Ce_{0.8}Gd_{0.2}O_{2-\delta}$) to electronic conductor (the nominal $FeCo_2O_4$) was maintained at 85:15. To obtain homogeneous powder mixtures with different particle sizes, two different wet ball milling procedures were applied. For both cases, powder mixture, ethanol and zirconia balls were filled up to ~30 vol% in a polyethylene bottle. The weight ratio of powder : ball : ethanol was 1:2:3 as also described in [19]. The milling procedures were conducted on a roller bench. The first powder mixture (referred to as CF-1) was obtained through a one-step ball milling for 3 days, using 5 mm (diameter) zirconia balls. The second powder mixture (referred to as CF-2) was obtained through a two-step ball milling including a first step for 3 days using 5 mm (diameter) zirconia balls and a second step for 7 days using 1 mm (diameter) zirconia balls [19]. After drying at 75 °C for 3 days and sieved by a 150 µm-mesh sieve, the powder mixtures were uniaxially pressed into pellets at 19 MPa [19] and 50 MPa [18], respectively for powder CF-1 and CF-2.

In order to increase inhomogeneity and percolation of the minor compound (the nominal $FeCo_2O_4$) but maintain a constant weight ratio of $Ce_{0.8}Gd_{0.2}O_{2-\delta}$ to $FeCo_2O_4$ (i.e., 85:15) for powder mixture, a dry mixing method was used instead of the wet ball milling method. However, dry mixing of 85 wt% $Ce_{0.8}Gd_{0.2}O_{2-\delta}$ powders with 15 wt% nominal $FeCo_2O_4$ powders does not lead to sufficient percolation of the minor compound in the membrane but results in many isolated islands. Therefore, inhomogeneous powder mixtures were prepared by dry mixing of 50 wt% $Ce_{0.8}Gd_{0.2}O_{2-\delta}$ powders with composite powder having a nominal composition 70 wt% $Ce_{0.8}Gd_{0.2}O_{2-\delta}$:30 wt% $FeCo_2O_4$. The composite powder was prepared using the procedures as described for powder CF-2. The mixing process was conducted in a moderate manual way within a limited time of ~10 min so that most of Co_3O_4 and Fe_2O_3 will not blend into the monophase powder ($Ce_{0.8}Gd_{0.2}O_{2-\delta}$) but keep concentrated in the composite ceramic powders. With a comparable amount, the monophase powders and the composite ceramic powders are expected to retain well individual percolation on the mesoscale after being moderately mixed. The obtained inhomogeneous powder mixture (referred to as CF-D) was uniaxially pressed into pellets under 50 MPa.

All pellets were sintered in air at 1200 °C for 10 h; a slow cooling rate of 0.5 K/min was used between 900 °C and 800 °C [19], while the heating and cooling rate for the other temperature ranges was 3 K/min. The codes of the different membranes, obtained by solid-state reactive sintering, were the same as those of the powders, i.e. CF-1, CF-2 and CF-D.

The particle size distribution of precursor powders was determined by the laser diffraction method based on Mie theory using a Horiba LA 950 V2 analyzer (Retsch Technology GmbH, Haan, Germany). The specific surface area of precursor powders and powder mixtures was measured by the Brunauer-Emmett-Teller (BET) single-point method by low-temperature N_2 adsorption using Areameter II (Ströhlein Instruments, Viersen, Germany).

The powder mixtures were investigated by back scattered electron microscopy (BSEM) (Merlin, Carl Zeiss Microscopy, Oberkochen, Germany) regarding particle morphology, and by energy-dispersive X-ray spectroscopy (EDS) (Merlin, Carl Zeiss Microscopy, Oberkochen, Germany) with respect to elemental distributions. EDS investigations were carried out at 4 kV accelerating voltage using an X-Max 80 detector and the AZtec data acquisition and analysis software package (Oxford Instruments Nanoanalysis, High Wycombe, United Kingdom). Before the EDS investigation, the powder mixtures were mixed with epoxy resin. After the resin had hardened, the cross section was ground using 800-grit SiC paper, and then polished by argon ion milling for 8 h at 6 kV / 150 µA using a JEOL SM-09010 (JEOL Ltd., Tokyo, Japan) polisher.

Microstructures and phase constituents were investigated at the cross sections of the sintered membranes by scanning electron microscopy (SEM) (Merlin, Carl Zeiss Microscopy, Oberkochen, Germany) and electron backscatter diffraction (EBSD) (NordlysNano, Oxford Instruments, Wiesbaden, Germany), as well as EDS for element distribution. The area fraction of each phase was deduced by image analysis using the HKL Channel 5 software packages. The volume fraction was estimated to be equal to the area fraction for each phase in a random section through each composite [31]. The porosity was estimated as the area fraction of the pores using the ImageJ software [32].

The gas tightness of the sintered membrane was assessed using a He-leak detector (ASM 340, Pfeiffer Vaccum GmbH, Asslar, Germany). Helium was fed at one side of the membrane, while a vacuum was drawn on the other side. The helium flow gas passing through the sample was collected by the detector and calculated as helium leakage rate.

Oxygen permeation measurements were conducted using sintered pellets, which were polished at two sides to thicknesses of ~0.95 ± 0.02 mm and ground to diameters of ~14.65 ± 0.05 mm prior to gold sealing. Each pellet was sealed with a gold ring at each side in a glass tube setup at approx. 1020 °C for 5 hours under a spring load. Oxygen permeation flux in a steady-state was measured between approx. 1020 °C and 850 °C using air and argon as feed and sweep gas at a flow rate of 250 ml/min and 50 ml/min, respectively. The individual sample temperature was measured online with a thermocouple (type S). The thermocouple was placed in approx. 5 mm distance to the sample in radial direction so that the feed and sweep gas flows were not affected. The sample temperature can vary maximally by approx. 20 K from sample to sample and in particular between two identical furnaces operated in parallel. One

specimen of each of the bare CF-1, CF-2 and CF-D membrane types were assessed. In addition, oxygen permeation flux was also measured for the sintered pellets that are coated with surface activation layers. For that reason, the polished pellets were screen printed with a porous $La_{0.58}Sr_{0.4}Co_{0.2}Fe_{0.8}O_{3-\delta}$ (LSCF) coating at both sides, as described in [22], and then post-sintered at 1100 °C for 30 min. One coated CF-1, one coated CF-2 and two coated CF-D membranes were characterized.

3. Results and discussion

3.1 Powder characteristics

The microstructures of dual phase membranes, e.g., grain sizes and distributions of individual phases, are significantly affected by the sizes of particles, as well as agglomerates within precursor powders. Hence, the dimensions of particles and agglomerates are investigated in detail using different characterization methods.

Figure 1 provides the morphologies of the as-received precursor powders. Most of the particles exhibit quasi-spherical shapes, while the as-received Fe_2O_3 has few particles with irregular shapes (see Figure 1(b)). The homogeneity of particle sizes of the as-received precursor powders decreases in the order of Co_3O_4 > $Ce_{0.8}Gd_{0.2}O_{2-\delta}$ > Fe_2O_3. Notably, the as-received Co_3O_4 contains comparatively large round agglomerates (see Figure 1(d)), whereas it is relatively difficult to distinguish any agglomerates in the as-received $Ce_{0.8}Gd_{0.2}O_{2-\delta}$ and Fe_2O_3.

The specific surface areas of the as-received $Ce_{0.8}Gd_{0.2}O_{2-\delta}$, Fe_2O_3 and Co_3O_4 powders are measured to be ~7.9 m^2/g, ~5.8 m^2/g and ~3.3 m^2/g, respectively. The rather low specific surface area for the as-received Co_3O_4 reflects that the particle clusters, as can be seen in Figure 1(d), are hard agglomerates with low inner porosities.

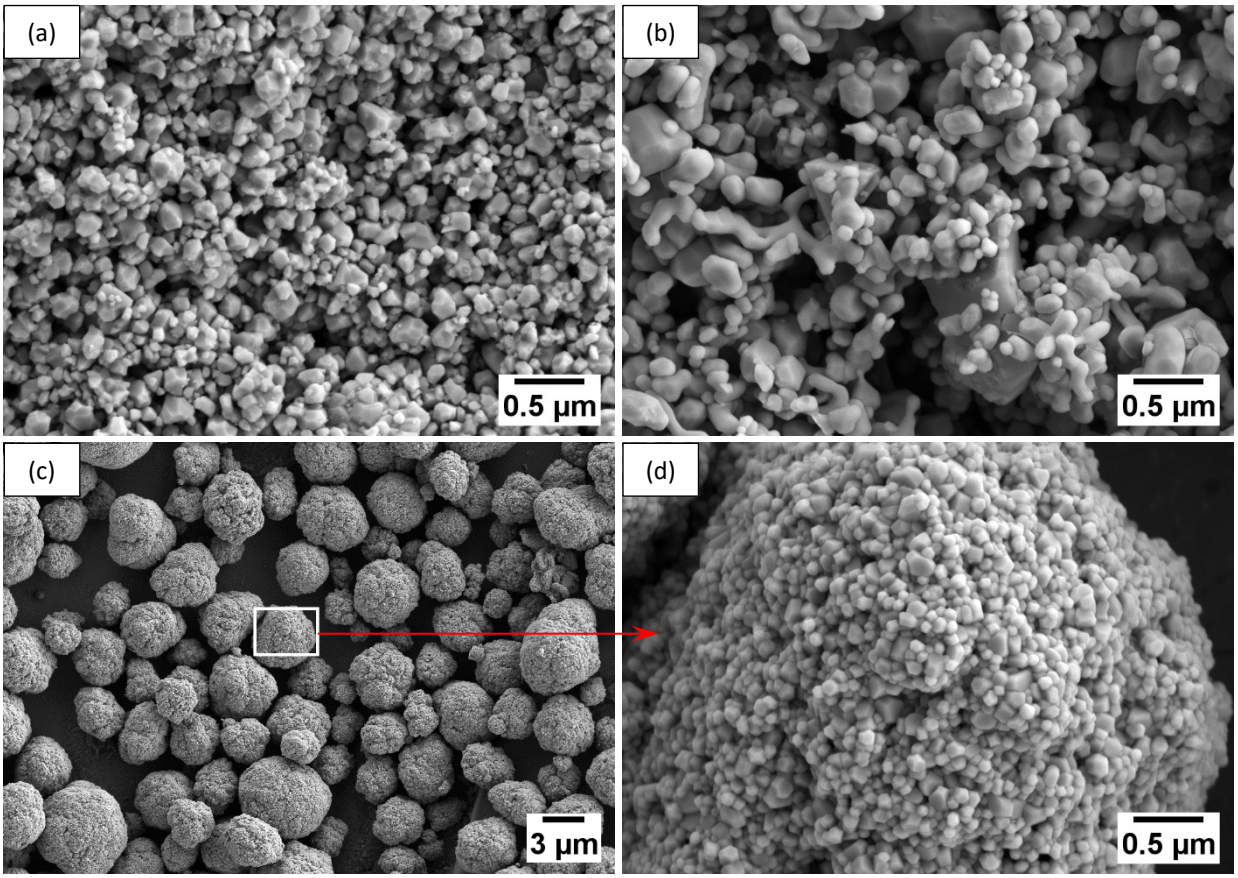

Figure 1 Particle morphologies of the as-received precursor powders: (a) $Ce_{0.8}Gd_{0.2}O_{2-\delta}$, (b) Fe_2O_3 and (c) Co_3O_4: (d) is a magnified view of the agglomerate framed in (c).

The laser diffraction method can provide a quantitative analysis of apparent particle sizes that can reflect the sizes of hard agglomerates. For the as-received $Ce_{0.8}Gd_{0.2}O_{2-\delta}$ powders, although the median apparent particle size d_{50} (~0.1 µm) is comparable to the average size of particles shown in Figure 1(a), the measured apparent particle sizes reflect the sizes of both particles and agglomerates indicated by the bimodal particle size distribution profile (see Figure 2(a)). The apparent particle size distribution becomes gradually tighter with increasing milling steps, while d_{50} hardly changes; the specific surface area of the as-received $Ce_{0.8}Gd_{0.2}O_{2-\delta}$ is slightly increased to ~10.6 m^2/g by the two-step milling process, which suggests that the reduction of apparent particle size is mainly attributed to the breaking of agglomerates.

For the as-received Fe_2O_3 powders, the apparent particle size distribution shows a unimodal profile (see Figure 2(b)), and the d_{50} is measured to be ~1.4 µm, which is larger than the sizes of the most particles shown in Figure 1(b), which implies the existence of a large number of big agglomerates. The d_{50} is not modified by the one-step milling process, but dramatically reduced to 0.53 µm by the two-step milling process although there are still few (< 20 vol%) particles with apparent sizes above 1 µm (see Figure

2(b)). These large particle sizes can possibly be the sizes measured for the remaining agglomerates. The specific surface areas of Fe_2O_3 is changed insignificantly.

For the as-received Co_3O_4 powders, the apparent particle sizes are distributed in a unimodal profile (see Figure 2(c)), with d_{50} is ~7.5 µm, which is noticeably close to the sizes of agglomerates (see Figure 1(c)), indicating that the agglomerates are very compact and do not break during the measurement. The d_{50} is reduced by one-step milling and two-step milling to ~3.0 µm and ~0.35 µm, respectively. The particle size distribution of the one-step milled Co_3O_4 powders shows a bimodal profile, while the two-step milled Co_3O_4 powders have a unimodal distribution profile (see Figure 2(c)). Although the specific surface area of the two-step milled Co_3O_4 is increased to 13.0 m^2/g, the d_{50} of the two-step milled Co_3O_4 is still larger than the size of the primary particle indicated in Figure 1(d). These observations indicate that large agglomerates in the as-received Co_3O_4 are milled into small agglomerates by two-step milling; the small agglomerates appear to be rather compact and cannot easily be shattered by ball milling.

Therefore, it can be concluded that the two-step milling method is an effective way to reduce the particle size and size distribution of the precursor powders. Such effects on different precursor powders decrease in the order of Co_3O_4 > $Ce_{0.8}Gd_{0.2}O_{2-\delta}$ > Fe_2O_3. A further increase of the milling time for the two-step milling procedure is verified to make no significant change regarding the apparent particle sizes (not shown here).

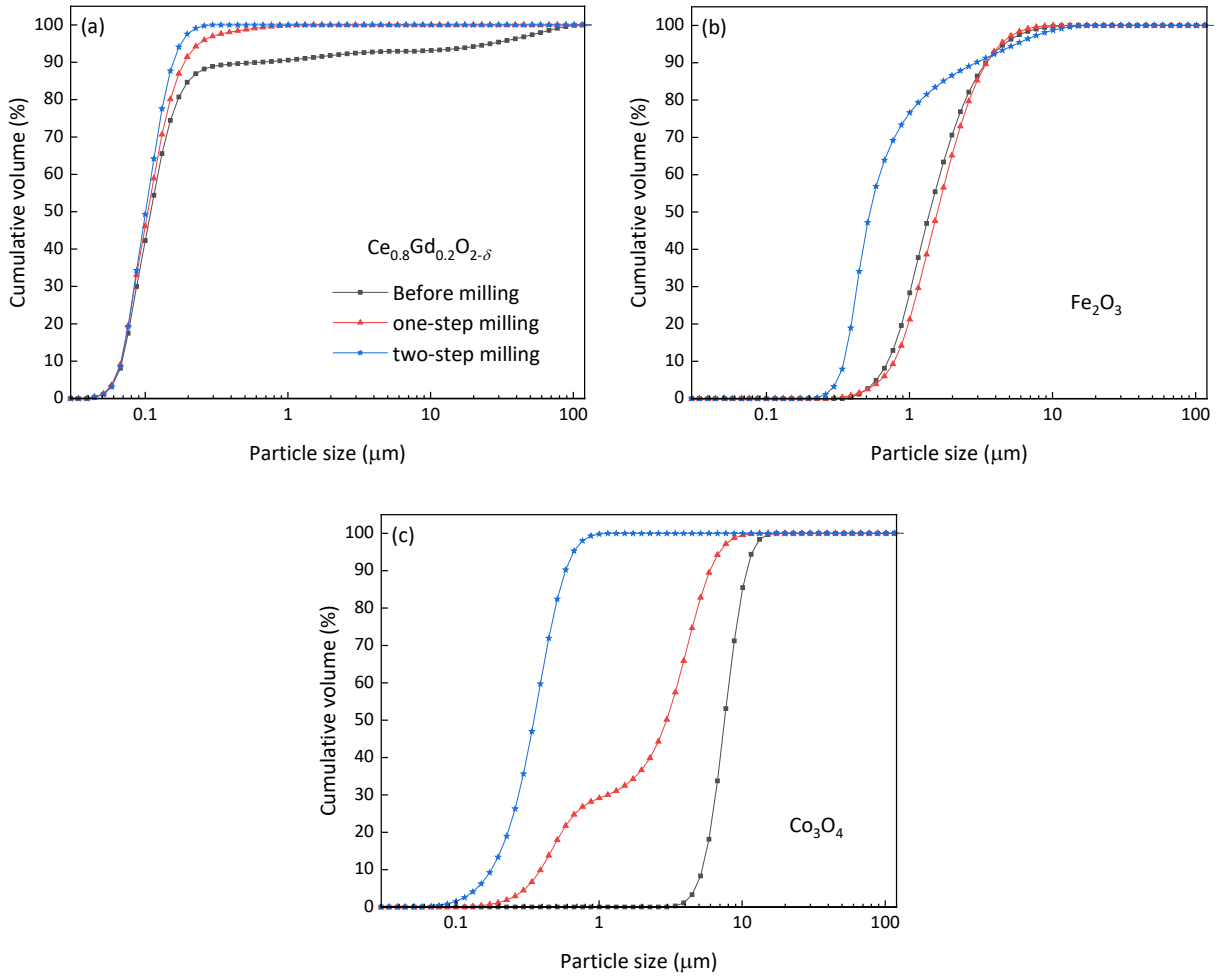

Figure 2 Particle size distributions of precursor powders before and after ball milling: (a) $Ce_{0.8}Gd_{0.2}O_{2-\delta}$, (b) Fe_2O_3 and (c) Co_3O_4. (the legends in (a) also apply to (b) and (c)).

To further investigate the effect of the different milling procedures on powder mixtures, the wet ball-milled powder mixtures were characterized by BSEM and EDS. As shown in Figure 3, Ce-rich, Fe-rich and Co-rich grains represent, respectively, $Ce_{0.8}Gd_{0.2}O_{2-\delta}$, Fe_2O_3 and Co_3O_4 particles. Large Co_3O_4 and Fe_2O_3 particles or agglomerates can be seen in the powder CF-1. By contrast, Co_3O_4 and Fe_2O_3 in the powder CF-2 exhibit small and homogenous particle sizes (see Figure 4). Fe_2O_3 shows larger particle sizes than Co_3O_4 in the powder CF-2. No obvious agglomerates are found in the powder CF-2. The specific surface areas are 8.2 m^2/g and 13.8 m^2/g, respectively, for the powder CF-1 and CF-2. These results suggest that agglomerates can be shattered by the two-step milling procedure for the precursor powders milled together.

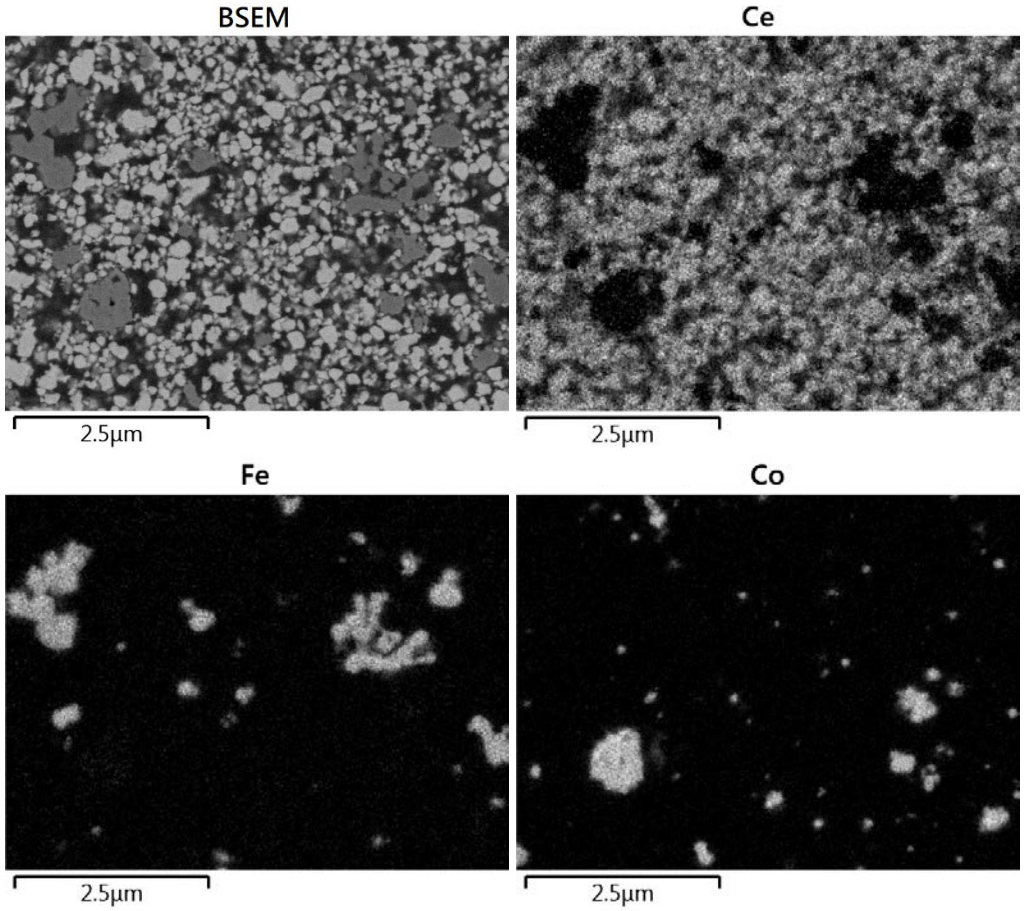

Figure 3 BSEM micrograph and corresponding EDS elements mapping on the powder CF-1 embedded in epoxy resin. Ce-rich, Fe-rich and Co-rich grains represent, respectively, $Ce_{0.8}Gd_{0.2}O_{2-\delta}$, Fe_2O_3 and Co_3O_4 particles.

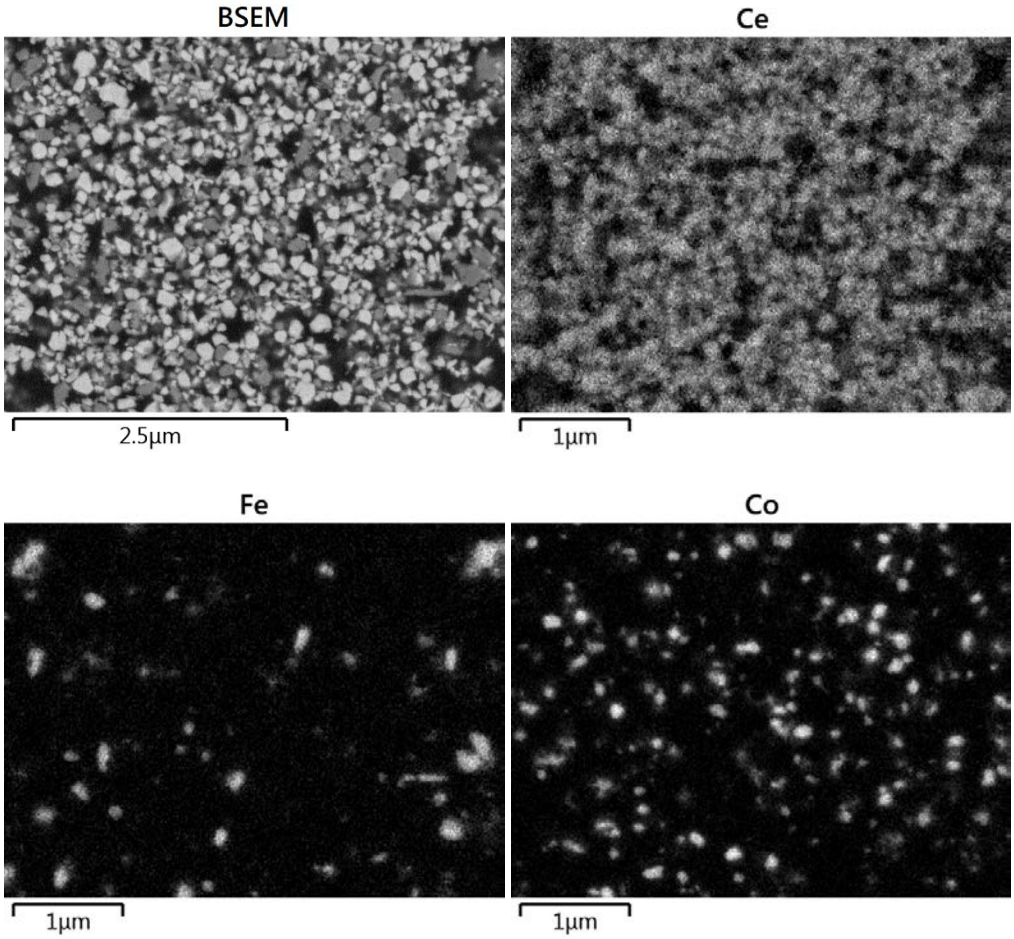

Figure 4 BSEM micrograph and the corresponding EDS elements mapping on the powder CF-2 embedded in epoxy resin. Ce-rich, Fe-rich and Co-rich grains represent, respectively, $Ce_{0.8}Gd_{0.2}O_{2-\delta}$, Fe_2O_3 and Co_3O_4 particles.

3.2 Phase and microstructure characterizations

The microstructure and phase constituents of the membranes prepared by the wet ball-milled powder mixtures are shown in Figure 5. The closed porosities of CF-1 and CF-2 are below ~2 %. The grains that appear black in Figure 5(a, c) are FCO or CoO according to the EBSD phase mapping (see Figure 5(b, d)), while the grey and light grey grains are CGO and GCFCO, respectively. The FCO grains are well dispersed within the CGO phase. The grain size of FCO in CF-1 shows a large variation due to the existence of a high amount of large grains (see Figure 5 (a, b)). The CoO phase is a residue from sintering, which should be re-oxidized to the spinel structure during cooling. The CoO phase is only detected in CF-1 (see Figure 5(b)). Apparently, the re-oxidation of the large grains in CF-1 would need more time and, thus, is not completed. Obviously, the one-step milling process is much less effective compared to the two-step milling process resulting in a coarse microstructure.

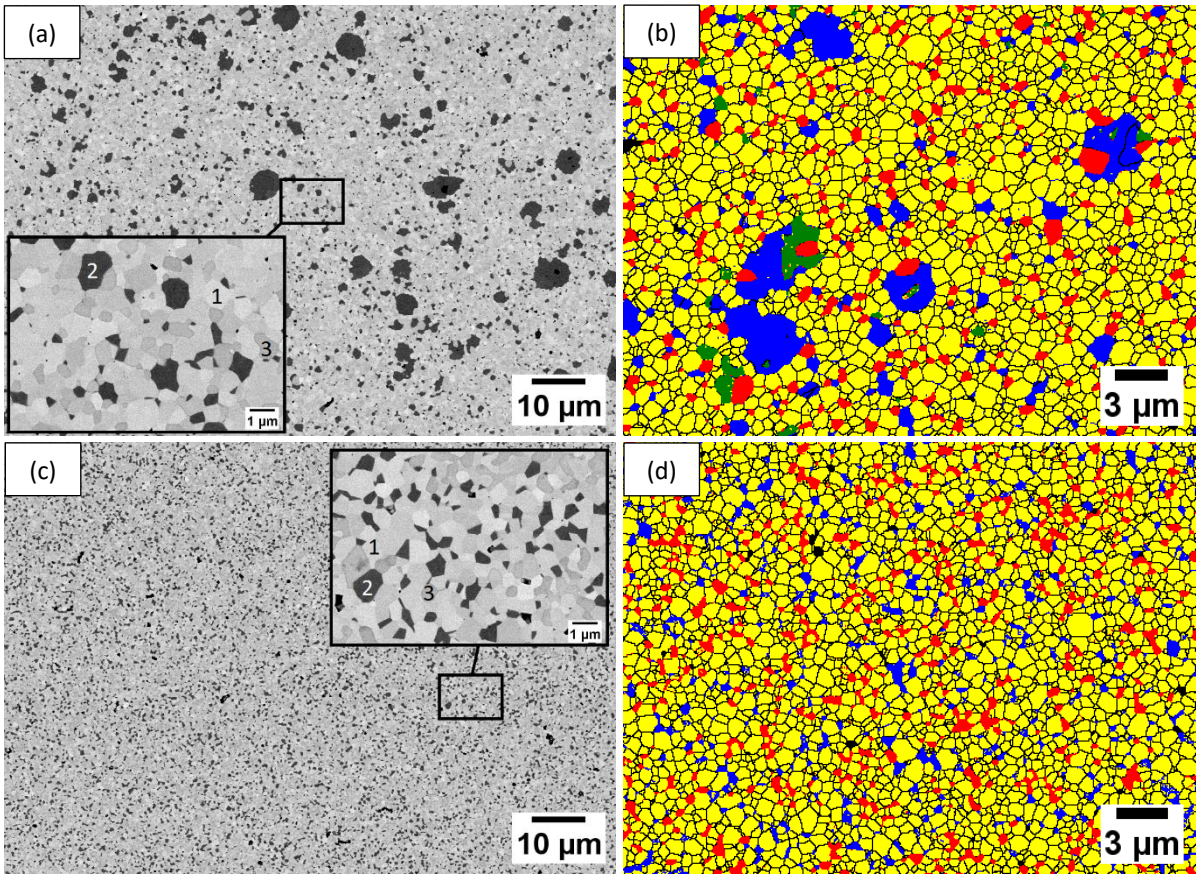

Figure 5 BSEM micrographs (left column: a, c) and EBSD phase mapping (right column: b,d) of (a,b) CF-1 and (c,d) CF-2. In the SEM micrographs, the grains denoted as 1, 2, 3 represent CGO, FCO (or CoO) and GCFCO grains, respectively. In the EBSD phase mapping, the yellow, blue, red and green phases are CGO, FCO, GCFCO and CoO, respectively, while the black spots and dark lines are pores and grain/phase boundaries, respectively.

Furthermore, EDS reveals the existence of Co-rich phases at the grain boundaries of CGO or GCFCO in CF-1, as shown in Figure 6. The Ce-rich, Gd-rich and Co-rich grains represent, respectively, the CGO, GCFCO and FCO (or CoO) grains, while the Fe-rich grains can be either GCFCO or FCO (or CoO) grains. The FCO grains mainly contain Co and Fe, and the GCFCO grains consist of Gd and Fe, as well as very little Ce and Co. A little amount of Co seems to segregate along the grain boundaries of CGO or GCFCO forming a grain boundary phase, which appears to create a connection between two isolated FCO grains and potentially provide paths for electronic conduction along the grain boundaries but may hinder ionic conduction across the grain boundaries [33].

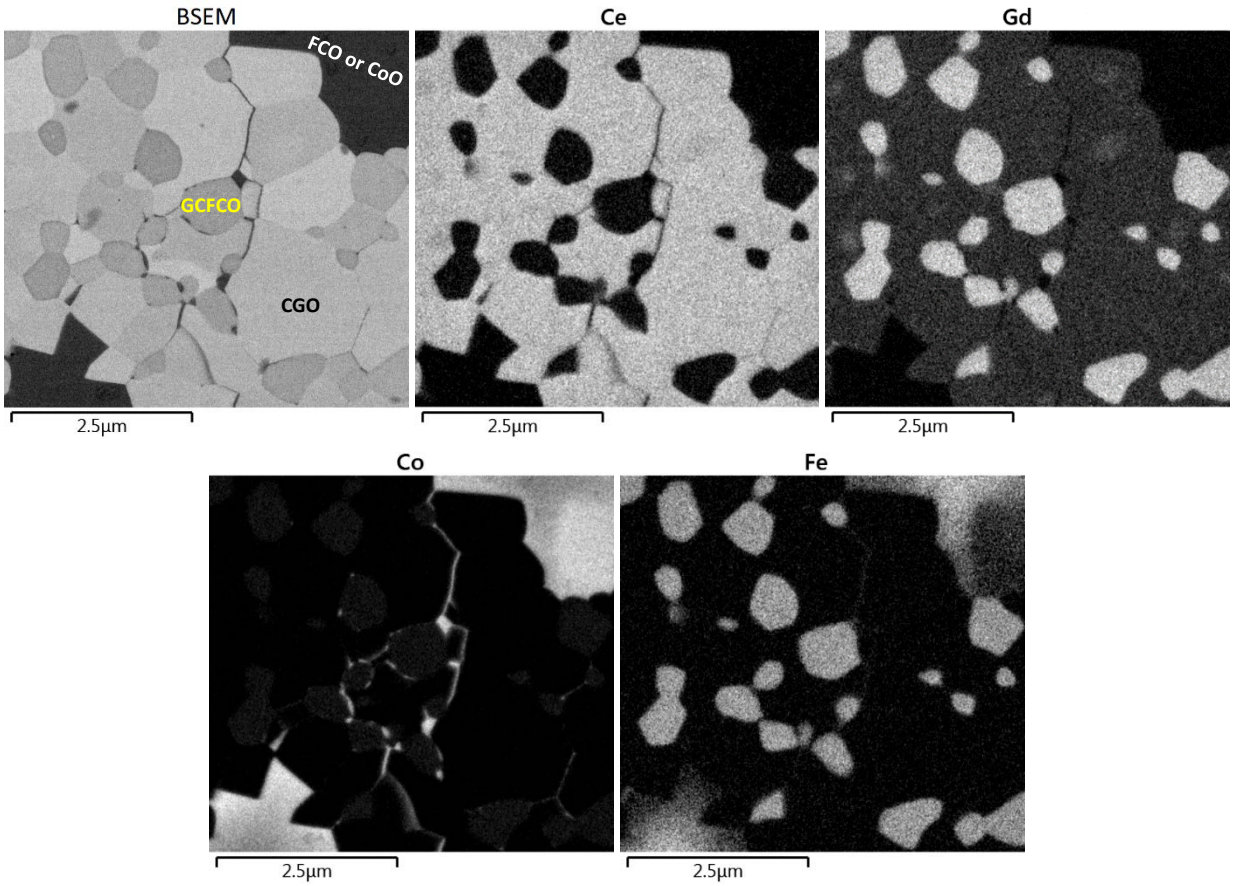

Figure 6 BSEM micrograph and the corresponding EDS element mapping on CF-1. The Ce-rich, Gd-rich and Co-rich grains represent, respectively, the CGO, GCFCO and FCO (or CoO) grains, while the Fe-rich grains can be either GCFCO or FCO (or CoO) grains.

By contrast, for CF-D, the FCO and CoO grains are noticeably only distributed in one specific zone, and have rather small grain size variation (see Figure 7(a)); phase areas in CF-D can be well distinguished as a monophase zone and a multiphase zone (see Figure 7(b)). The different zones are well connected on the mesoscale with connections between the larger regions, rather than having connections only between distributed grains. The phase distributions are considerably homogenous in the multiphase zone in CF-D (see Figure S1 (a)), which is much like the one reported for 70 wt% $Ce_{0.8}Gd_{0.2}O_{2-\delta}$:30 wt% $FeCo_2O_4$ membrane [34]. The multiphase zone appears to have fewer pores than the monophase zone (see Figure S1), which benefits from the phase interactions between CGO and FCO during sintering. These phase interactions result in the formation of the GCFCO phase, and dominate the densification process [19]. The monophase zone, which mainly comprises pure CGO, suffers from low sintering activity leading to small but closed porosity (Figure S1(b)). In addition, few defects, e.g., cracks and voids (marked by arrows in Figure 7(a)), are found in the monophase zone and interfaces between different zones, but the membrane is still gastight as verified by the low helium leakage rate (< 10^{-8} mbar·L·s^{-1}).

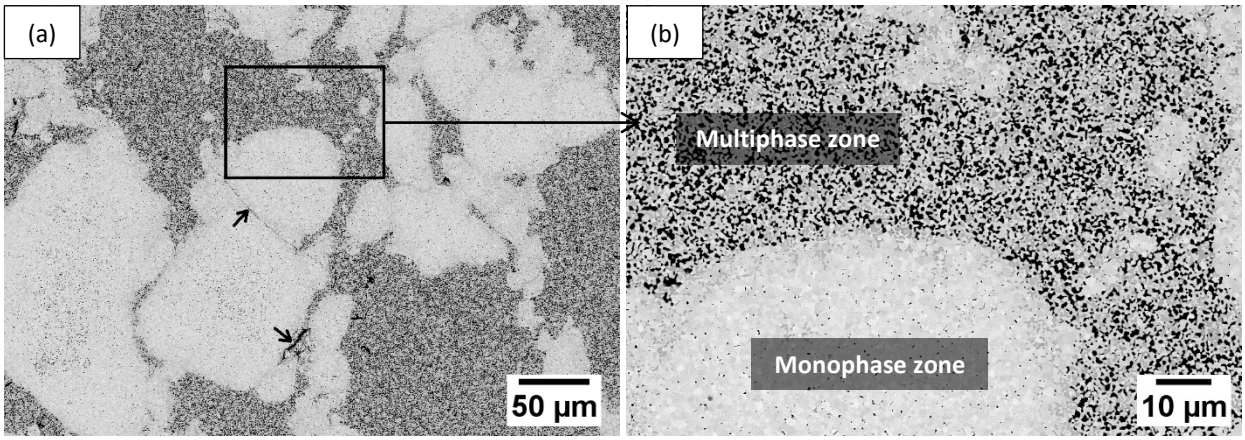

Figure 7 BSEM micrographs of CF-D. Only few defects exist and are indicated by arrows in (a). Two zones consisting of a different number of phases are observed, i.e., multiphase and monophase zones, as labeled in (b).

The phase constituents in the different zones within CF-D are analyzed in detail by EBSD. As shown in Figure 8, CGO, FCO, GCFCO and CoO phases are observed in CF-D. Few GCFCO grains are located at the interface between the monophase zone and the multiphase zone (see Figure 8(a)). This is an indication of elements diffusion and phase interactions between the different zones, which contributes to obtaining a robust interface and a dense microstructure.

The multiphase zone contains four different phases as expected (see Figure 8(b)). Microscale percolations of ionic conducting phase (i.e., CGO) and electronic conducting phases (i.e., FCO, CoO and GCFCO [18, 26]) can be observed (see Figure 8(b)). By contrast, the monophase zone mainly consists of CGO phase (see Figure 8(c)). The EDS point quantification results suggest that the average Ce/Gd ratio in CGO in the monophase zone is close to the one in pure $Ce_{0.8}Gd_{0.2}O_{2-\delta}$ (see Table S1), but lower than the one in the multiphase zone. The depletion of Gd content in CGO in the multiphase zone is caused by the formation of GCFCO [18]. It also indicates that the Gd content in the different zones has not been homogenized through mixing or diffusion under the current sintering conditions, because the diffusion pathways might be too long.

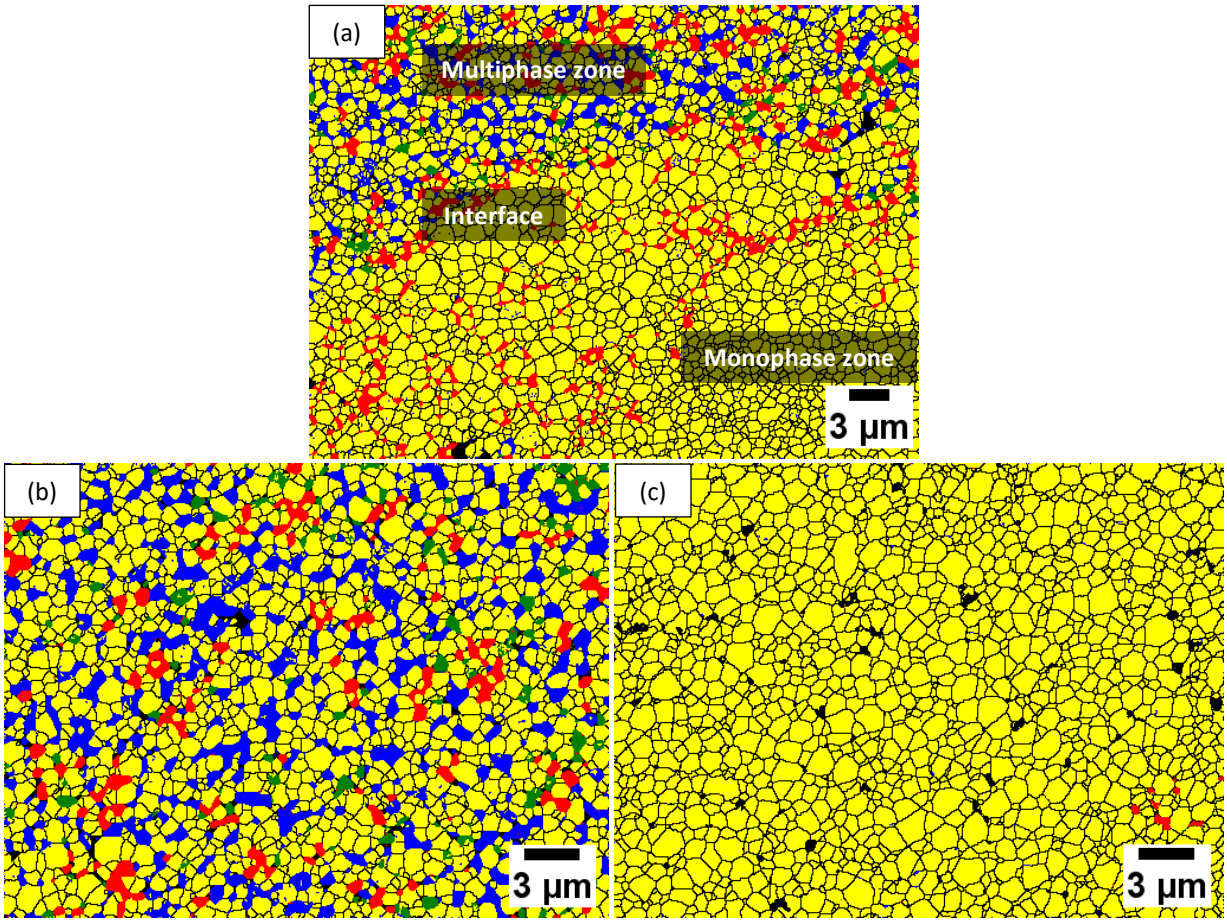

Figure 8 EBSD phase mapping of CF-D: (a) overview, (b) multiphase zone and (c) monophase zone: the yellow, blue, red and green phases are CGO, FCO, GCFCO and CoO, respectively, while the black spots and dark lines are pores and grain/phase boundaries, respectively.

Volumetric quantifications were determined based on the average of three different areas investigated by EBSD for each membrane and each phase zone; the sizes of the areas investigated were the same as the ones exemplarily shown in Figure 5(b, d) and Figure 8 (b, c). Among these phase constituents, only CGO shows ionic conductivity, and hence, contributes to the ionic conduction during oxygen permeation, while FCO, CoO and GCFCO are good electronic conductors and responsible for electronic conduction [18, 26]. A result of a scan is shown in Table 1, the amount of ionic/electronic conducting phase in CF-1 and CF-2 is comparable, and electronic conducting phases are characterized to possess a minor volume.

By contrast, phase amounts are fairly different in the two phase zones in CF-D, as shown in Table 1. The monophase zone in CF-D can be regarded as pure CGO phase despite the existence of a small amount of FCO, GCFCO and CoO. The amount of electron conducting phases is almost two times higher in the multiphase zone in CF-D than in either CF-1 or CF-2, representing the original 70 wt% $Ce_{0.8}Gd_{0.2}O_{2-\delta}$:30 wt% $FeCo_2O_4$ powder mixture. This reveals that the concept of using a pure ionic conducting phase and a

mixed ionic-electronic conducting composite with high electronic conductivity to form a novel "dual phase" works from the microstructural point of view.

Table 1 Volume fractions of individual phases in the sintered membranes.

Sample		Ionic conducting phase	Electronic conducting phase			
		CGO (vol %)	FCO (vol %)	GCFCO (vol %)	CoO (vol %)	Sum (vol %)
CF-D	CF-1	81.1	8.5	9.8	0.6	18.9
	CF-2	82.3	7.6	10.1	-	17.7
	Monophase zone	99.7	0.1	0.1	0.1	0.3
	Multiphase zone	68.4	19.9	7.9	3.9	31.6

3.3 Oxygen permeation

The helium leakage rates of all sintered membranes are determined to be below 10^{-8} mbar·L·s^{-1}, which confirms dense microstructures that are sufficient for oxygen permeation measurements.

The oxygen permeance, i.e., oxygen permeation flux (see Figure S3) normalized by the oxygen partial pressure gradient (see equation (4)) as a function of temperature [15], was determined via:

$$Permeance = \frac{J_{O_2}}{\ln \frac{P'_{O_2}}{P''_{O_2}}} \tag{4}$$

where J_{O_2} is the oxygen permeation flux; P'_{O_2} and P''_{O_2} are oxygen partial pressure of oxygen rich and lean side of the membrane.

For the coated membranes, the limiting effect from surface exchange is believed to be overcome by an LSCF coating so that oxygen permeation process is merely limited by bulk diffusion, the oxygen permeance can be expressed as [18, 35]:

$$Permeance = \frac{R}{16 \cdot F^2} \cdot \frac{1}{L} \cdot \sigma_{amb} \cdot T \tag{5}$$

where T is the temperature, R the gas constant, L the thickness of the membrane, F the Faraday constant. At a fixed temperature, σ_{amb} is a constant, hence, oxygen permeance tends to increase with decreasing thickness according to equation (5). The activation energy of oxygen permeance is

independent of thickness but equal to the activation energy of bulk diffusion represented by $\sigma_{amb} \cdot T$, which can be described by an Arrhenius approach.

The cross section of the coated membrane is shown in Figure 9 for CF-D as an example. A ~4 μm thick porous coating was successfully synthesized at the surface of CF-D. The coating possesses an LSCF perovskite structure as revealed by XRD (see Figure S2). The EDS mapping at the interface (see Figure S3) indicates no significant element diffusion between the coating and substrate. Similar coatings were also prepared for CF-1 and CF-2.

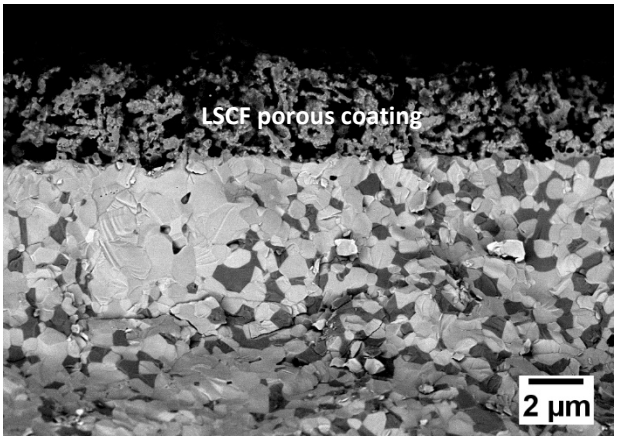

Figure 9 Cross section of the coated CF-D.

For the coated CF-D, average oxygen fluxes (see Figure S4) were obtained, and the experimental errors for each oxygen flux value are ~±2 %, the upper and lower bounds of which represent oxygen fluxes of two samples. The temperature difference between the two samples is less than 7 K, i.e. <0.7%, for each data point. For other membranes, the experimental errors of oxygen fluxes were estimated to be the same due to the same test conditions and the reproducible microstructures.

The oxygen permeances of the coated membranes, as provided in Figure 10, increase in the order of CF-1 < CF-2 < CF-D which indicates that the limiting effect from bulk diffusion decreases following CF-1 > CF-2 > CF-D.

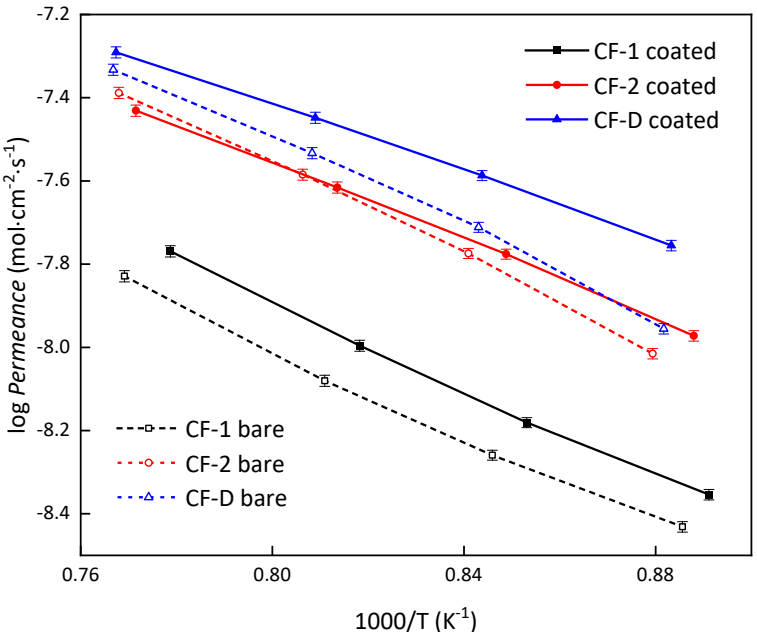

Figure 10 Oxygen permeances of the sintered membranes with an average thickness of ~0.95 ± 0.02 mm.

When compared with the oxygen flux reported for the LSCF coated 85 wt% $Ce_{0.8}Gd_{0.2}O_{2-\delta}$-15 wt% $FeCo_2O_4$ composite prepared by a Pechini process [15], the oxygen fluxes of the coated CF-D are lower as can be seen from Table 2. It should be noted that these results were obtained under the same test conditions and similar sample dimensions. It indicates that the microstructure obtained by the Pechini process is advantageous for preparing a better performing dual phase membrane. However, the Pechini process involves expensive raw materials, significant NO_x emissions, and is difficult to scale up. By contrast, the solid-state reactive sintering process we used contains facile treatments of commercially available precursor powders, which benefits for a feasible upscaling production. For commercialization, a balance of processing efforts and performance benefits has to be found.

Table 2 Comparison of oxygen fluxes of the membranes prepared by different methods.

Preparation methods	J_{O_2} (mL·cm^{-2}·min^{-1})		Reference
	850 °C	900 °C	
Pechini	0.16	0.20	[15]
Solid-state reactive sintering	0.11	0.15	This work (the coated CF-D)

The activation energy (E_a) of oxygen permeance was calculated from the Arrhenius plot of oxygen permeance for each membrane, as listed in Table 3. In contrast to the oxygen permeance, E_a values for the coated membranes decrease in an order CF-1 > CF-2 > CF-D. The E_a value of the coated CF-D is

nearly the same as the E_a value of ionic conductivity of $Ce_{0.8}Gd_{0.2}O_{2-\delta}$ (~79 kJ/mol [16]), which suggests that the ionic conduction within CGO is the rate-limiting steps in the coated CF-D. The E_a value of the coated CF-2 is marginally higher than the E_a value of ionic conductivity of $Ce_{0.8}Gd_{0.2}O_{2-\delta}$. Nevertheless, it can still be indicative that the ionic conduction within CGO is the permeation rate-limiting steps in the coated CF-2, but the ionic conductivity of CGO in CF-2 is lower than that of $Ce_{0.8}Gd_{0.2}O_{2-\delta}$, which can be attributed to the depletion of Gd within CGO, after phase interactions. Since such phase interactions only occur at the multiphase zone in CF-D, the composition of CGO in the monophase zone is close to that of $Ce_{0.8}Gd_{0.2}O_{2-\delta}$, ensuring fast ionic conduction. In comparison, the E_a value of the coated CF-1 is close to the E_a value of electronic conductivity of $FeCo_2O_4$ (~102 kJ/mol [15]), suggesting the electronic conduction within FCO is the rate-limiting step.

Table 3 Activation energies of oxygen permeances of the sintered membranes.

Sample	E_a (kJ/mol)	
	bare	coated
CF-1	99 ± 5	100 ± 4
CF-2	107 ± 4	89 ± 2
CF-D	103 ± 5	77 ± 2

These results emphasize the importance of the microstructure in a composite, in particular when the phase ratio is in the range where the transition of the rate-limiting mechanism from ionic to electronic conduction occurs. Although the volume of electronic conducting phases is almost the same in all samples, the total number of grains of the electronic conducting phases is lower in CF-1 than in CF-2 due to the existence of large FCO grains (see Figure 5(a)). Considering each grain of electronic conducting phases as one unit in continuous electronic conducting networks, it is harder to form long-range free paths for electronic conduction in CF-1 than in CF-2. The best percolations of ionic conducting phase and electronic conducting phases are formed in CF-D through, respectively, the monophase zone and the multiphase zone.

Possible diffusion paths through each membrane are illustrated and compared in Figure 11. The electronic conduction in CF-1 might partially rely on the Co-rich grain boundary phases, which bridge the neighbouring grains of electronic conducting phases, but only provides limited electronic conduction due to a bottleneck effect. As a consequence, CF-1 tends to possess the lowest performance, although the volume fraction of ionic/electronic conducting phases within CF-1 and CF-2 is similar (see Table 1). Such a blocking effect on electronic conduction is overcome in the CF-2 by an increased amount of robust electronic conductive paths through smaller grains (see Figure 11(b)), providing a higher effective electronic conductivity. Since the intrinsic electronic conductivity of $FeCo_2O_4$ is almost two orders higher

than the intrinsic ionic conductivity of CGO [26], once there are robust paths for conducting electrons, the bulk diffusion is limited by the ionic conductivity through the CGO.

CF-D appears to have more free paths for electronic conduction with lesser tortuosity since the small grains of electronic conducting phases are concentrated in the multiphase zone and closer to each other (see Figure 11(c)). More importantly, CGO within the monophase zone, which can be regarded as $Ce_{0.8}Gd_{0.2}O_{2-\delta}$ and has a somewhat higher ionic conductivity than the Gd-depleted CGO within CF-2, provides rather straight conductive paths dominating the ionic conduction within CF-D. Therefore, CF-D shows the highest performance, in particular when the porous LSCF coating distributes electrons on the surface instantaneously suppressing surface exchange limitations.

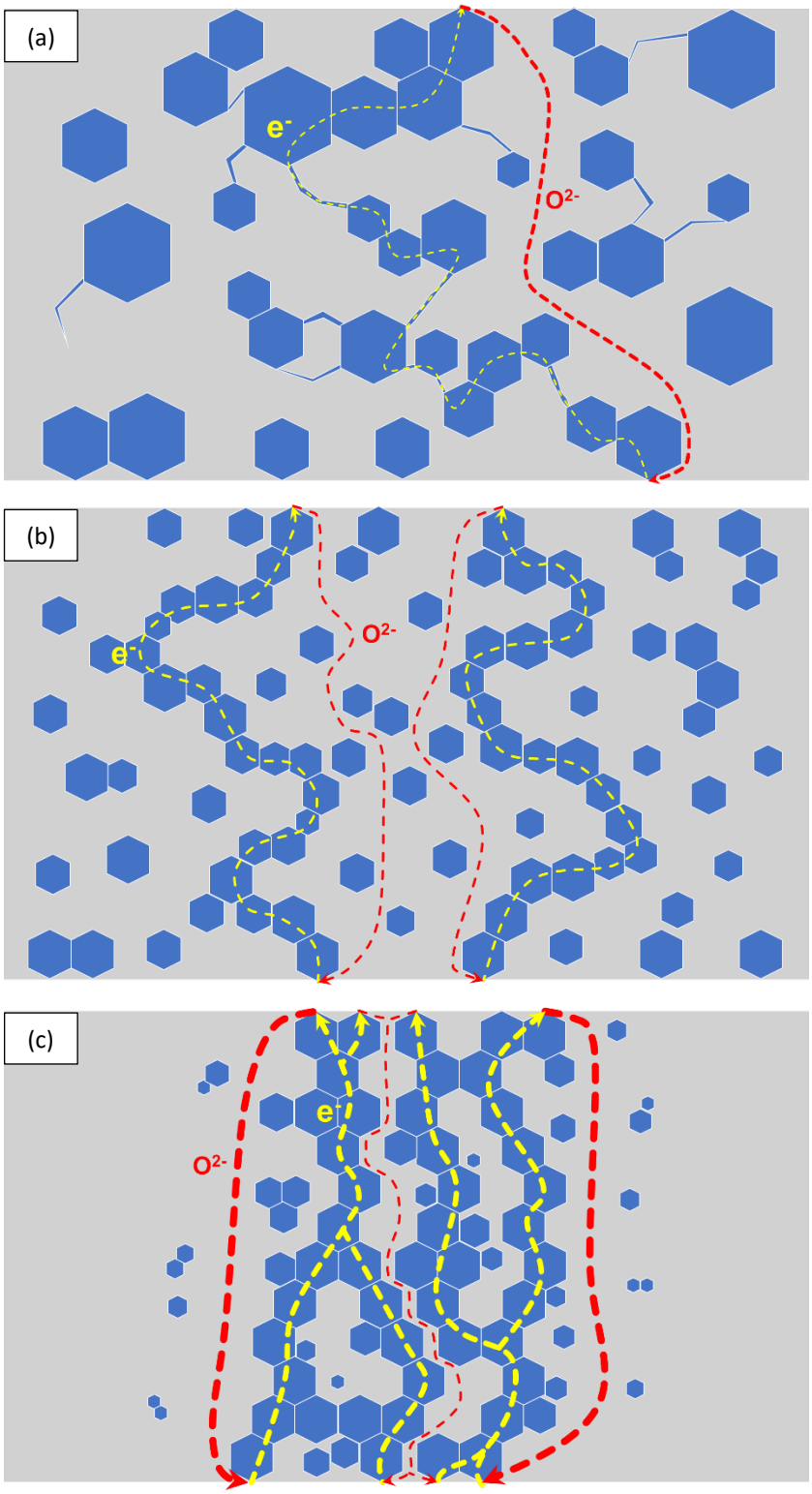

Figure 11 Schematic illustrating oxygen ion diffusion paths (red dashed lines) through ionic conducting phase (grey background) and electrons diffusion paths (yellow dashed lines) through electronic conducting phases (blue hexagons) in (a) CF-1, (b) CF-2 and (c) CF-D. The thicker lines represent better paths with less tortuosity.

For the bare membranes, the oxygen permeances of CF-D are slightly higher than that of CF-2 but remarkably higher than that of CF-1 (see Figure 10), which suggests that both surface exchange and bulk diffusion are faster during oxygen permeation in CF-2 and CF-D than in CF-1. The oxygen permeances of the bare CF-1 and the bare CF-D are lower than that of the coated CF-1 and the coated CF-D, respectively, over the entire temperature range due to the sluggish surface exchange [22], while the oxygen permeances of the bare CF-2 are marginally lower than that of the coated CF-2 below ~950 °C. This reflects the existence of limitations from the surface exchange during the oxygen permeation within the bare membranes. It is noteworthy that for CF-2 the improvement of oxygen permeance by LSCF coating is relatively low. This indicates that the surface exchange at the bare surface of CF-2 is relatively fast related to the fine and homogeneous microstructures providing long TPBs at the surface.

The bare samples share similar high E_a values (see Table 3), indicating the same permeation rate-limiting factors. The E_a value of the bare CF-1 is comparable to that of the coated CF-1, while the E_a values of the bare CF-2 and the bare CF-D are larger than that of the coated CF-2 and the coated CF-D, respectively, indicating different permeation rate-limiting steps, i.e., increased surface exchange influence [15].

Although the E_a values of the bare membranes are close to that of electronic conductivity of $FeCo_2O_4$, it is unlikely that the electronic conductivity becomes rate-limiting. It is rather likely that the oxygen permeance is controlled by both surface exchange and bulk diffusion, which is investigated by comparing two different membrane thicknesses.

When the limiting effects from surface exchange are not negligible, the oxygen permeance is reduced according to [35]:

$$Permeance = \frac{1}{1+\frac{2\cdot L_c}{L}}\cdot\frac{R}{16\cdot F^2}\cdot\frac{1}{L}\cdot\sigma_{amb}\cdot T \qquad (6)$$

where L_c is the characteristic thickness, defined as the thickness where oxygen permeation process experiences equal resistance from bulk diffusion and surface exchange [36]. When $L_c \ll L$, the limiting effect from surface exchange is negligible, hence, bulk diffusion is the major rate-limiting factor, and equation (6) can be simplified leading to equation (5). However, when L is in the vicinity of L_c, the limiting effects from surface exchange are nonnegligible, and oxygen permeance and its activation energy are then sensitive to thickness changes [35].

Figure 12 compares oxygen permeances of two bare CF-2 membranes with different thicknesses. Although the thickness difference is small (~0.2 mm), the change of oxygen permeance, as well as its activation energy, are significant. The oxygen permeance is improved when the thickness is reduced as expected according to equation (5), and the improvement is more significant at high temperatures, correlated with the increase of the activation energy. The bare 0.76 mm thick membrane has a higher activation energy of oxygen permeance indicating an increased limiting effect from surface exchange compared to the 0.96 mm thick membrane. For the bare 0.96 mm thick CF-2 membrane, the activation energy of oxygen permeance is smaller, but still higher than that of the coated CF-2 membrane (see Table 3).

It can be concluded that for the bare CF-2 the oxygen permeation is controlled by both surface exchange and bulk diffusion in the investigated region of thickness and temperature. With activation energy of oxygen permeance similar to that of the bare CF-2, the bare CF-1 and CF-D, are expected to suffer from the same multiple bottlenecks during oxygen permeation as the bare CF-2. The surface exchange characteristics of composites need further attention because it is not only an intrinsic material property but dependent on the length of TPBs present at the surface and, thus, again microstructure dependent.

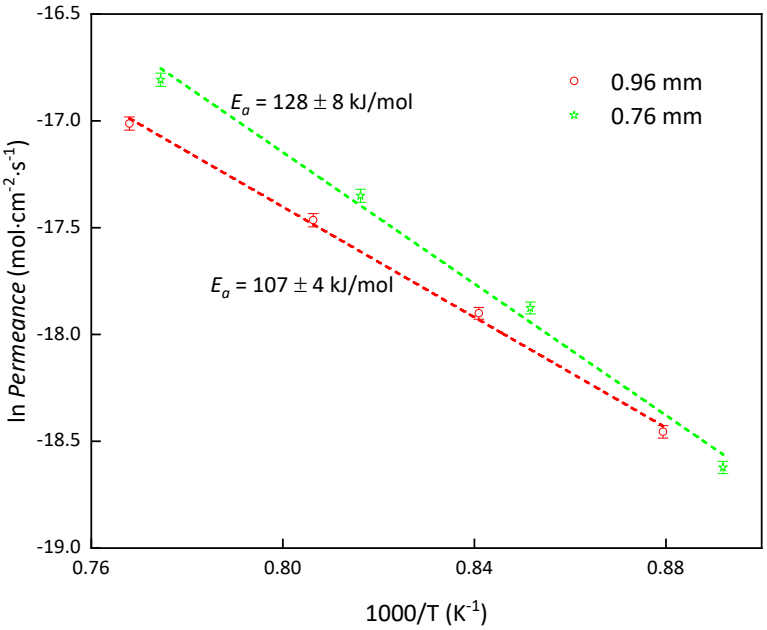

Figure 12 Arrhenius plot of oxygen permeances of the bare CF-2 membranes with different thicknesses.

Given that the coated CF-D exhibits the highest oxygen permeance, the stability of the coated CF-D was investigated. One coated CF-D sample was operated for 335 h at 863 ± 1 °C using the same test conditions as described in the experimental section; the gas analysis was stopped twice for recalibration of the mass spectrometer. As presented in Figure 13, the oxygen permeation flux of the coated CF-D first experiences a slight decrease of ~4 % from the initial state or from the initial state after each recalibration within a relatively short time (less than 40 h), then remained constant at ~96 % of the initial value.

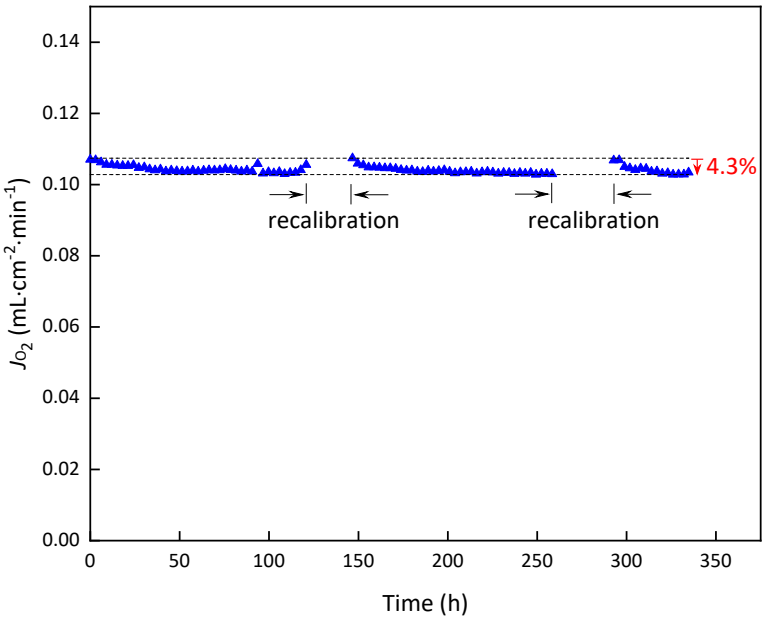

Figure 13 Oxygen permeation flux of the coated CF-D at 863 ± 1 °C as a function of time.

After operation for this long-term oxygen permeation test, the sample was fractured to reveal the cross section for further investigations. When compared with the cross section of the fresh sample, the cross section at the argon side of the measured sample shows no significant difference in microstructure (as can be seen by comparing Figure 14(a) and Figure 9) or elemental distribution (see Figure S3 and Figure S5). However, the cross section at the air side of the measured sample (see Figure 14(b)) exhibits different characteristics: several grains segregate out of the multiphase zone at the interface between membrane and activation layer. These grains appear to be FCO grains since they mainly contain Fe and Co (as revealed by EDS mapping shown in Figure S6). Such phase segregation was also observed for the same composite prepared by a Pechini process [15], and was reported to have a limited influence on oxygen permeation in the measured time frame [15]. Similarly, the segregated FCO grains at the air side shown here have not caused a significant decrease in oxygen permeation flux over 335 h as shown in Figure 13.

Therefore, considering the fact that the oxygen permeation flux of the coated CF-D stabilizes at around 96 % of the initial value after an operation time > 300 h despite the phase segregation, a rather stable performance regarding oxygen permeation can be concluded for the CF-D.

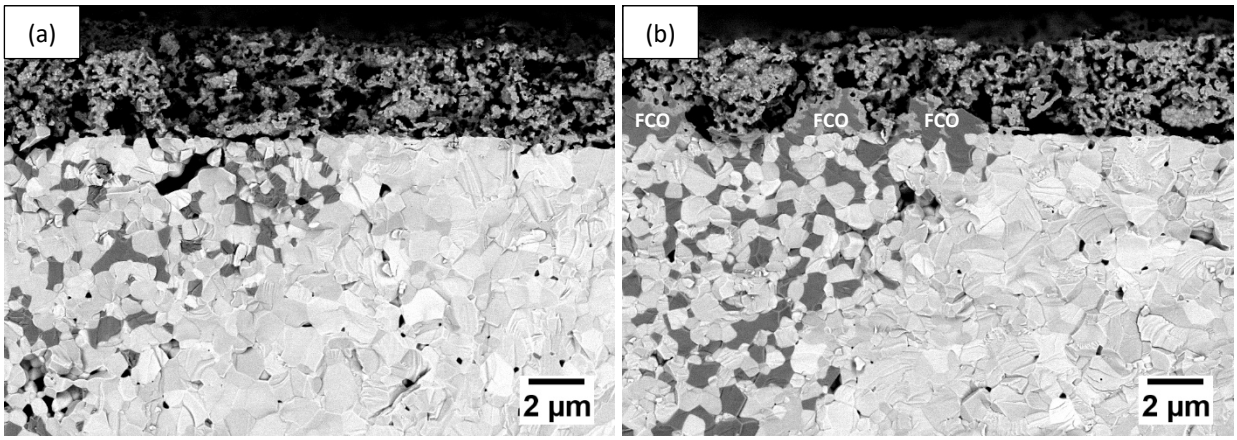

Figure 14 Cross sections at the (a) argon and the (b) air sides of the coated CF-D after a long-term (over 300 h) permeation test.

4 Conclusions

85 wt% $Ce_{0.8}Gd_{0.2}O_{2-\delta}$: 15 wt% $FeCo_2O_4$ composites were prepared by solid-state reactive sintering using powder mixture containing $Ce_{0.8}Gd_{0.2}O_{2-\delta}$, Co_3O_4 and Fe_2O_3 as precursor powders. Different powder preparation methods were used to synthesize membranes with varied microstructural characteristics.

The results reveal that homogenous microstructures were obtained using the powder mixtures prepared by the traditional ball milling method. The particle sizes of powder mixtures are reduced gradually with increasing milling time and reduction of the ball size due to the improved crushing effect on agglomerates. The reduced particle sizes of powder mixtures contribute to sintering a membrane with a fine and homogeneous microstructure, which exhibits higher oxygen permeance than the membrane with large grains due to good connections between ionic/electronic conducting phase and long TPBs at the surfaces. In comparison, a rather inhomogeneous microstructure with fine grains was sintered using inhomogeneous powder mixtures, which were prepared by dry mixing of $Ce_{0.8}Gd_{0.2}O_{2-\delta}$ powder with 70 wt% $Ce_{0.8}Gd_{0.2}O_{2-\delta}$:30 wt% $FeCo_2O_4$ powder resulting in the same nominal weight ratio 85:15 of $Ce_{0.8}Gd_{0.2}O_{2-\delta}$ and $FeCo_2O_4$. The fine but inhomogeneous microstructure exhibits two clearly distinguishable and percolating phase zones: one monophase zone mainly consists of $Ce_{0.8}Gd_{0.2}O_{2-\delta}$, permitting fast ionic conduction through relatively straight paths, and a multiphase zone contains both ionic and electronic conducting phases, providing mixed ionic-electronic conductivity with high electronic conduction through robust paths. Such a novel microstructure results in the highest oxygen permeance.

We present the successful synthesis of such a novel “dual phase” membrane containing a pure ionic conducting phase and a mixed ionic-electronic conducting composite with high electronic conductivity, which demonstrates how the limiting effect on bulk diffusion caused by unfavorable microstructural characteristics can be overcome. Further improvements are expected by using alternative ionic conducting compounds with high intrinsic ionic conductivity.

Acknowledgements

Fanlin Zeng acknowledges the China Scholarship Council (CSC) for his scholarship. The authors gratefully acknowledge Dr. E. Wessel, Dr. D. Grüner, Mr. M. Ziegner, Mr. S. Heinz, Ms. S. Schwartz-Lückge and Ms. A. Hilgers for structural characterization and property testing.

References

[1] X. Bi, X. Meng, P. Liu, N. Yang, Z. Zhu, R. Ran, S. Liu, A novel CO_2-resistant ceramic dual-phase hollow fiber membrane for oxygen separation, J. Membr. Sci. 522 (2017) 91-99. DOI: https://doi.org/10.1016/j.memsci.2016.09.008.
[2] C. Li, W. Li, J.J. Chew, S. Liu, X. Zhu, J. Sunarso, Oxygen permeation through single-phase perovskite membrane: Modeling study and comparison with the dual-phase membrane, Sep. Purif. Technol. 235 (2020) 116224. DOI: https://doi.org/10.1016/j.seppur.2019.116224.
[3] M. Czyperek, P. Zapp, H.J.M. Bouwmeester, M. Modigell, K.V. Peinemann, I. Voigt, W.A. Meulenberg, L. Singheiser, D. Stöver, MEM-BRAIN gas separation membranes for zero-emission fossil power plants, Energy Procedia 1 (2009) 303-310. DOI: https://doi.org/10.1016/j.egypro.2009.01.042.
[4] M. Czyperek, P. Zapp, H.J.M. Bouwmeester, M. Modigell, K. Ebert, I. Voigt, W.A. Meulenberg, L. Singheiser, D. Stöver, Gas separation membranes for zero-emission fossil power plants: MEM-BRAIN, J. Membr. Sci. 359 (2010) 149-159. DOI: https://doi.org/10.1016/j.memsci.2010.04.012.
[5] J. Garcia-Fayos, J.M. Serra, M.W.J. Luiten-Olieman, W.A. Meulenberg, 8-Gas separation ceramic membranes, in: O. Guillon (Ed.), Advanced Ceramics for Energy Conversion and Storage, Elsevier, 2020, pp. 321-385.
[6] J. Garcia-Fayos, M. Balaguer, J.M. Serra, Dual-Phase Oxygen Transport Membranes for Stable Operation in Environments Containing Carbon Dioxide and Sulfur Dioxide, ChemSusChem 8 (2015) 4242-4249. DOI: https://doi.org/10.1002/cssc.201500951.
[7] S. Baumann, J.M. Serra, M.P. Lobera, S. Escolástico, F. Schulze-Küppers, W.A. Meulenberg, Ultrahigh oxygen permeation flux through supported $Ba_{0.5}Sr_{0.5}Co_{0.8}Fe_{0.2}O_{3-\delta}$ membranes, J. Membr. Sci. 377 (2011) 198-205. DOI: https://doi.org/10.1016/j.memsci.2011.04.050.
[8] J.M. Serra, J. Garcia-Fayos, S. Baumann, F. Schulze-Küppers, W.A. Meulenberg, Oxygen permeation through tape-cast asymmetric all-$La_{0.6}Sr_{0.4}Co_{0.2}Fe_{0.8}O_{3-\delta}$ membranes, J. Membr. Sci. 447 (2013) 297-305. DOI: https://doi.org/10.1016/j.memsci.2013.07.030.
[9] B. Wei, Z. Lü, S. Li, Y. Liu, K. Liu, W. Su, Thermal and Electrical Properties of New Cathode Material $Ba_{0.5}Sr_{0.5}Co_{0.8}Fe_{0.2}O_{3-\delta}$ for Solid Oxide Fuel Cells, Electrochem. Solid-State Lett. 8 (2005) A428. DOI: https://doi.org/10.1149/1.1951232.
[10] S.R. Bishop, K.L. Duncan, E.D. Wachsman, Thermo-Chemical Expansion in Strontium-Doped Lanthanum Cobalt Iron Oxide, J. Am. Ceram. Soc. 93 (2010) 4115-4121. DOI: https://doi.org/10.1111/j.1551-2916.2010.03991.x.
[11] C. Zhang, J. Sunarso, S. Liu, Designing CO_2-resistant oxygen-selective mixed ionic-electronic conducting membranes: guidelines, recent advances, and forward directions, Chem. Soc. Rev. 46 (2017) 2941-3005. DOI: https://doi.org/10.1039/C6CS00841K.
[12] J.H. Joo, K.S. Yun, C.-Y. Yoo, J.H. Yu, Novel oxygen transport membranes with tunable segmented structures, Journal of Materials Chemistry A 2 (2014) 8174-8178. DOI: https://doi.org/10.1039/C4TA01271B.
[13] K. Zhang, Z. Shao, C. Li, S. Liu, Novel CO_2-tolerant ion-transporting ceramic membranes with an external short circuit for oxygen separation at intermediate temperatures, Energy & Environmental Science 5 (2012) 5257-5264. DOI: https://doi.org/10.1039/C1EE02539B.

[14] K.S. Yun, C.-Y. Yoo, S.-G. Yoon, J.H. Yu, J.H. Joo, Chemically and thermo-mechanically stable LSM-YSZ segmented oxygen permeable ceramic membrane, J. Membr. Sci. 486 (2015) 222-228. DOI: https://doi.org/10.1016/j.memsci.2015.03.049.
[15] M. Ramasamy, E.S. Persoon, S. Baumann, M. Schroeder, F. Schulze-Küppers, D. Görtz, R. Bhave, M. Bram, W.A. Meulenberg, Structural and chemical stability of high performance $Ce_{0.8}Gd_{0.2}O_{2-\delta}$-$FeCo_2O_4$ dual phase oxygen transport membranes, J. Membr. Sci. 544 (2017) 278-286. DOI: https://doi.org/10.1016/j.memsci.2017.09.011.
[16] Y. Lin, S. Fang, D. Su, K.S. Brinkman, F. Chen, Enhancing grain boundary ionic conductivity in mixed ionic-electronic conductors, Nature Communications 6 (2015) 6824. DOI: https://doi.org/10.1038/ncomms7824.
[17] H. Luo, H. Jiang, T. Klande, F. Liang, Z. Cao, H. Wang, J. Caro, Rapid glycine-nitrate combustion synthesis of the CO_2-stable dual phase membrane $40Mn_{1.5}Co_{1.5}O_{4-\delta}$-$60Ce_{0.9}Pr_{0.1}O_{2-\delta}$ for CO_2 capture via an oxy-fuel process, J. Membr. Sci. 423-424 (2012) 450-458. DOI: https://doi.org/10.1016/j.memsci.2012.08.046.
[18] F. Zeng, J. Malzbender, S. Baumann, M. Krüger, L. Winnubst, O. Guillon, W.A. Meulenberg, Phase and microstructural characterizations for $Ce_{0.8}Gd_{0.2}O_{2-\delta}$-$FeCo_2O_4$ dual phase oxygen transport membranes, J. Eur. Ceram. Soc. 40 (2020) 5646-5652. DOI: https://doi.org/10.1016/j.jeurceramsoc.2020.06.035.
[19] F. Zeng, J. Malzbender, S. Baumann, A. Nijmeijer, L. Winnubst, M. Ziegner, O. Guillon, R. Schwaiger, W.A. Meulenberg, Optimization of sintering conditions for improved microstructural and mechanical properties of dense $Ce_{0.8}Gd_{0.2}O_{2-\delta}$-$FeCo_2O_4$ oxygen transport membranes, J. Eur. Ceram. Soc. (2020). DOI: https://doi.org/10.1016/j.jeurceramsoc.2020.09.009.
[20] F. Zeng, J. Malzbender, S. Baumann, W. Zhou, M. Ziegner, A. Nijmeijer, O. Guillon, R. Schwaiger, W.A. Meulenberg, Mechanical reliability of $Ce_{0.8}Gd_{0.2}O_{2-\delta}$-$FeCo_2O_4$ dual phase membranes synthesized by one-step solid-state reaction, J. Am. Ceram. Soc. 00 (2020) 1-17. DOI: https://doi.org/10.1111/jace.17583.
[21] X. Zhu, W. Yang, Mixed conducting ceramic membranes, Springer-Verlag, Berlin, Germany, 2017.
[22] M. Ramasamy, S. Baumann, J. Palisaitis, F. Schulze-Küppers, M. Balaguer, D. Kim, W.A. Meulenberg, J. Mayer, R. Bhave, O. Guillon, M. Bram, Influence of Microstructure and Surface Activation of Dual-Phase Membrane $Ce_{0.8}Gd_{0.2}O_{2-\delta}$-$FeCo_2O_4$ on Oxygen Permeation, J. Am. Ceram. Soc. 99 (2016) 349-355. DOI: https://doi.org/10.1111/jace.13938.
[23] X. Zhu, H. Wang, W. Yang, Relationship between homogeneity and oxygen permeability of composite membranes, J. Membr. Sci. 309 (2008) 120-127. DOI: https://doi.org/10.1016/j.memsci.2007.10.011.
[24] Q. Li, X. Zhu, Y. He, Y. Cong, W. Yang, Effects of sintering temperature on properties of dual-phase oxygen permeable membranes, J. Membr. Sci. 367 (2011) 134-140. DOI: https://doi.org/10.1016/j.memsci.2010.10.045.
[25] Z. Fan, A.P. Miodownik, P. Tsakiropoulos, Microstructural characterisation of two phase materials, Mater. Sci. Technol. 9 (1993) 1094-1100. DOI: https://doi.org/10.1179/mst.1993.9.12.1094.
[26] M. Ramasamy, S. Baumann, A. Opitz, R. Iskandar, J. Mayer, D. Udomsilp, U. Breuer, M. Bram, Phase Interaction and Distribution in Mixed Ionic Electronic Conducting Ceria-Spinel Composites, Advances in Solid Oxide Fuel Cells and Electronic Ceramics II: Ceramic Engineering and Science Proceedings Volume 37, Issue 3 37 (2017) 99-112. DOI: https://doi.org/10.1002/9781119320197.ch9.
[27] U. Pippardt, J. Boeer, C. Bollert, A. Hoffmann, M. Heidenreich, R. Kriegel, M. Schulz, A. Simon, Performance and stability of mixed conducting composite membranes based on substituted ceria, J. Ceram. Sci. Technol. 5 (2014) 309-316. DOI: https://doi.org/10.4416/JCST2014-00014.

[28] H. Takamura, K. Okumura, Y. Koshino, A. Kamegawa, M. Okada, Oxygen Permeation Properties of Ceria-Ferrite-Based Composites, J. Electroceram. 13 (2004) 613-618. DOI: https://doi.org/10.1007/s10832-004-5167-y.
[29] H. Li, X. Zhu, Y. Liu, W. Wang, W. Yang, Comparative investigation of dual-phase membranes containing cobalt and iron-based mixed conducting perovskite for oxygen permeation, J. Membr. Sci. 462 (2014) 170-177. DOI: https://doi.org/10.1016/j.memsci.2014.03.047.
[30] X. Zhu, Y. Liu, Y. Cong, W. Yang, $Ce_{0.85}Sm_{0.15}O_{1.925}$-$Sm_{0.6}Sr_{0.4}Al_{0.3}Fe_{0.7}O_3$ dual-phase membranes: One-pot synthesis and stability in a CO_2 atmosphere, Solid State Ionics 253 (2013) 57-63. DOI: https://doi.org/10.1016/j.ssi.2013.08.040.
[31] A.J. Schwartz, M. Kumar, B.L. Adams, D.P. Field, Electron backscatter diffraction in materials science, Springer, New York, USA, 2009.
[32] C.A. Schneider, W.S. Rasband, K.W. Eliceiri, NIH Image to ImageJ: 25 years of image analysis, Nature Methods 9 (2012) 671-675. DOI: https://doi.org/10.1038/nmeth.2089.
[33] C. Kleinlogel, L.J. Gauckler, Sintering and properties of nanosized ceria solid solutions, Solid State Ionics 135 (2000) 567-573. DOI: https://doi.org/10.1016/S0167-2738(00)00437-9.
[34] F. Zeng, J. Malzbender, S. Baumann, F. Schulze-Küppers, M. Krüger, A. Nijmeijer, O. Guillon, W.A. Meulenberg, Micromechanical Characterization of $Ce_{0.8}Gd_{0.2}O_{2-\delta}$-$FeCo_2O_4$ Dual Phase Oxygen Transport Membranes, Adv. Eng. Mater. 22 (2020) 1901558. DOI: https://doi.org/10.1002/adem.201901558.
[35] J.H. Joo, G.S. Park, C.-Y. Yoo, J.H. Yu, Contribution of the surface exchange kinetics to the oxygen transport properties in $Gd_{0.1}Ce_{0.9}O_{2-\delta}$-$La_{0.6}Sr_{0.4}Co_{0.2}Fe_{0.8}O_{3-\delta}$ dual-phase membrane, Solid State Ionics 253 (2013) 64-69. DOI: https://doi.org/10.1016/j.ssi.2013.08.038.
[36] C. Li, W. Li, J.J. Chew, S. Liu, X. Zhu, J. Sunarso, Rate determining step in SDC-SSAF dual-phase oxygen permeation membrane, J. Membr. Sci. 573 (2019) 628-638. DOI: https://doi.org/10.1016/j.memsci.2018.12.044.